ATLAS CONF Note

ATLAS-CONF-2019-015

27th May 2019

Search for squarks and gluinos in final states with same-sign leptons and jets using 139 fb^{-1} of data collected with the ATLAS detector

The ATLAS Collaboration

A search for supersymmetric partners of gluons and quarks is presented, involving signatures with jets and either two isolated leptons (electrons or muons) with the same electric charge, or at least three isolated leptons. A data sample of proton–proton collisions at $\sqrt{s}$ = 13 TeV recorded with the ATLAS detector at the Large Hadron Collider between 2015 and 2018, corresponding to a total integrated luminosity of 139 fb^{-1}, is used for the search. No significant excess over the Standard Model expectation is observed. The results are interpreted in simplified supersymmetric models featuring both R-parity conservation and R-parity violation, extending the exclusion limits from previous searches up to 1600 GeV for gluino masses and 750 GeV for bottom and top squark masses in these scenarios.

ATLAS-CONF-2019-015
28 May 2019

1 Introduction

Experimental searches for manifestations of beyond Standard Model (BSM) physics at hadron colliders have long exploited the signature of final states comprising a pair of isolated light leptons (electrons, muons) with the same electric charge ("same-sign leptons"). New, heavy BSM particles which may be produced in proton–proton (pp) collisions often couple to massive Standard Model (SM) bosons or top quarks into which they decay. Signatures with same-sign leptons and jets may then often arise with significant branching ratios. Pair production of heavy BSM Majorana fermions may be another abundant source of events with same-sign leptons [1]. In the SM, production of prompt same-sign lepton pairs from weak boson decays is rare. In the context of $\sqrt{s} = 13$ TeV pp collisions, the inclusive cross-section is of the order of 1 pb [2, 3], thus suppressed by more than three orders of magnitude with respect to the production of opposite-sign lepton pairs.

At the Large Hadron Collider (LHC) [4], signatures with same-sign prompt leptons have been used by the ATLAS [5] and CMS [6] experiments to explore the landscape of possible SM extensions and their phenomenology. Among these proposed extensions, Supersymmetry (SUSY) [7–12] stands out as a particularly compelling framework. It was shown [13–16] to favourably impact the scale evolution of perturbative gauge couplings needed for a Grand Unification, and can address the SM gauge hierarchy problem. In its minimal realisation, the MSSM [17, 18], each fundamental SM fermion is associated with a pair of new scalar partners — in the case of quarks q, the squarks $\tilde{q}_L$ and $\tilde{q}_R$. Similarly, each SM bosonic degree of freedom is partenered with a new fermion. Mixing between the partners of SM electroweak and Higgs bosons[1] results in four massive Majorana fermions and two massive charged fermions (neutralinos $\tilde{\chi}_1^0$ to $\tilde{\chi}_4^0$ and charginos $\tilde{\chi}_1^\pm$ and $\tilde{\chi}_2^\pm$, indexed by increasing mass). The gluinos $\tilde{g}$, partners of the SM gluons, do not mix due to their colour charge.

The stability of the lightest superpartner (LSP), which is the consequence of an extra ad-hoc discrete symmetry, can provide viable candidates to explain Dark Matter in terms of weakly-interacting massive particles [19, 20]. When this symmetry, called R-parity [21], is conserved, supersymmetric partners can only be produced in pairs and decay into the LSP and SM particles, possibly in several steps via superpartners of intermediate masses. The LSP, stable and weakly interacting, escapes the detector leaving a striking experimental signature of large missing momentum. When R-parity is not conserved, the final states contain only SM particles; decay channels for squarks include e.g. $\tilde{q}_i \to q_j q_k$ or $\tilde{q}_i \to q_j \ell_k$, if the corresponding coupling strengths [22] λ''_{ijk} or λ'_{ijk} are non-zero.

Naturalness arguments [23, 24] suggest that the top squark mass may not exceed $\approx$ 1 TeV [25, 26]. Significant mixing between the two scalar top partners, enhanced with respect to other quark flavours, can also lower the mass of the lightest eigenstate $\tilde{t}_1$ below that of other squarks. These constraints affect indirectly gluinos and bottom squark masses as well. Gluinos and third-generation squarks may therefore be among the lightest superpartners and copiously produced at the LHC. Typical pair-production cross-sections [27] for interesting scenarios in the context of this note are 0.09 pb for 1.6 TeV gluino masses, or 0.33 pb for the lightest top $\tilde{t}_1$ or bottom $\tilde{b}_1$ squark masses at 800 GeV.

This note presents a search for gluinos and squarks in final states with two same-sign leptons and jets. Events may include additional leptons. Large missing transverse momentum is also required in the case of R-parity conserving models. The event selection also relies on the number of b-tagged jets. Simple signal regions (SRs) are built (Section 4) from a set of requirements on the kinematic properties of the selected events, in order to isolate the signature of supersymmetric processes from SM backgrounds. The

[1] The Higgs sector is also enriched by the presence of an additional complex doublet.

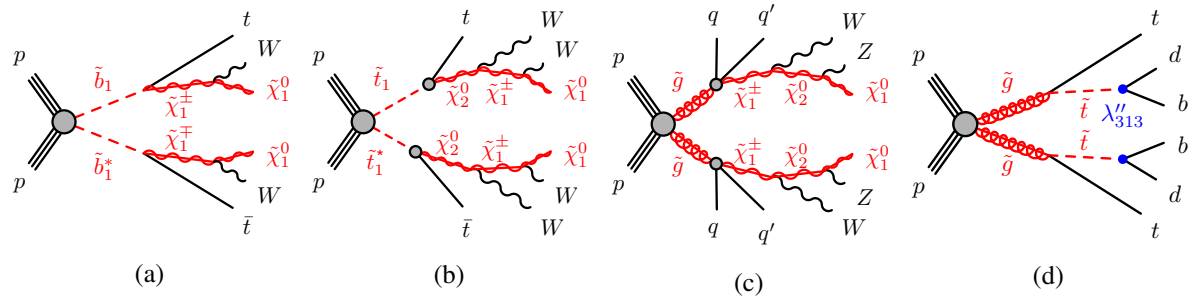

Figure 1: Examples of processes allowed in the MSSM, involving the pair-production and cascade decays of squarks and gluinos into final states with leptons and jets.

latter are estimated with Monte Carlo simulation for processes such as $t\bar{t}V$ or VV ($V = W, Z$) leading to prompt same-sign leptons (Section 5), while sources of same-sign leptons arising from jets misidentified as leptons or non-prompt leptons from decays of hadrons, as well as other reducible backgrounds, are estimated with data (Section 6). Event yields in data are then compared to the estimated contributions from SM processes. Results are presented for 139 fb^{-1} of 13 TeV pp collision data recorded by the ATLAS experiment in Section 7. They are interpreted in terms of exclusion limits (Section 8) on the parameters of four benchmark supersymmetric signal scenarios, which are shown in Figure 1.

A similar, earlier analysis, realised on a subset of the data for these results, was reported in Ref. [28] and found no deviation from the SM expectations. Searches based on these event topologies were also performed in the same context with the CMS experiment with the same outcome [29, 30].

2 ATLAS detector

The ATLAS experiment [5] at the LHC is a multi-purpose particle detector with a forward-backward symmetric cylindrical geometry and a near 4π coverage in solid angle.[2] It consists of an inner tracking detector (ID) surrounded by a thin superconducting solenoid providing a 2 T axial magnetic field, electromagnetic (EM) and hadron calorimeters, and a muon spectrometer (MS). The ID covers the pseudorapidity range $|\eta| < 2.5$. It consists of silicon pixel, silicon microstrip, and transition radiation tracking detectors, completed by the insertable B-layer (IBL) installed before Run 2 [31, 32]. Lead/liquid-argon (LAr) sampling calorimeters provide EM energy measurements with high granularity. A hadron (steel/scintillator-tile) calorimeter covers the central pseudorapidity range $|\eta| < 1.7$. The end-cap and forward regions are instrumented with LAr calorimeters for both EM and hadronic energy measurements up to $|\eta| = 4.9$. The MS surrounds the calorimeters and is based on three large air-core toroidal superconducting magnets with eight coils each. The field integral of the toroids ranges between 2.0 and 6.0 T·m. across most of the detector. The MS includes a system of precision tracking chambers and fast detectors for triggering. A two-level trigger system is used to select events. The first-level trigger is implemented in hardware and uses a subset of the detector information to reduce the accepted rate to at

[2] ATLAS uses a right-handed coordinate system with its origin at the nominal interaction point (IP) in the centre of the detector and the z-axis along the beam pipe. The x-axis points from the IP to the centre of the LHC ring, and the y-axis points upwards. Cylindrical coordinates r, ϕ are used in the transverse plane, ϕ being the azimuthal angle around the z-axis. The pseudorapidity is defined in terms of the polar angle θ as $\eta = -\ln\tan(\theta/2)$. The rapidity is defined relatively to the beam axis as a function of the velocity β: $y = 0.5 \times \ln\{(1+\beta\cos\theta)/(1-\beta\cos\theta)\}$. The magnitude of the momentum in the plane transverse to the beam axis is denoted as p_{T}.

most nearly 100 kHz. This is followed by a software-based trigger that reduces the accepted event rate to 1 kHz on average depending on the data-taking conditions.

3 Event reconstruction

The analysis is performed on a set of pp collision data recorded by the ATLAS detector between 2015 and 2018. In this period, the LHC delivered colliding beams with a peak instantaneous luminosity up to $L = 2.1 \times 10^{34}\text{cm}^{-2}\text{s}^{-1}$ achieved in 2018, and an average number of pp interactions per bunch crossing ('pile-up') of 33.7. After requirements on the stability of the beams, the operational status of all ATLAS detector components, and the quality of the recorded data, the total integrated luminosity of the dataset corresponds to 139 fb^{-1} with an uncertainty of 1.7%. It is derived from the calibration of the luminosity scale using x–y beam-separation scans, following a methodology similar to that detailed in Ref. [33], and using the LUCID-2 detector [34] for the baseline luminosity measurements.

Proton–proton interaction vertices are reconstructed from charged particle tracks in the ID with $p_{\text{T}} > 500$ MeV [35, 36]. The presence of at least one such vertex with a minimum of two associated tracks is required, and the primary vertex is chosen as the vertex with maximal sum of p_{T}^2 of associated tracks.

The anti-k_t algorithm [37] with radius parameter $R = 0.4$ implemented in the `FastJet` library [38] is used to reconstruct jets up to $|\eta| = 4.9$, relying on topological energy clusters in the calorimeter [39] at the EM scale. Jets are then calibrated as described in Ref. [40]. Only jets with $p_{\text{T}} > 20$ GeV are further considered. Events are vetoed when containing jets induced by calorimeter noise or non-collision background, according to criteria similar to those described in Ref. [41]. As decay products of heavy particles tend to be more central, this analysis only considers jets with $|\eta| < 2.8$ in multiplicity-based requirements. An additional discriminant referred to as the `Jet Vertex Tagger` (JVT) allows the exclusion of jets produced in pile-up processes [42], based on a classification of the tracks associated to the jet that do or do not point to the primary vertex.

Jets containing b-flavoured hadrons are identified in the region $|\eta| < 2.5$ by the MV2c10 b-tagging algorithm [43], which makes use of the impact parameters of tracks associated to the jet candidate, the position of reconstructed secondary vertices and their consistency with the decay chains of such hadrons. For the working point chosen for this analysis, such jets are tagged with an efficiency of 70% in simulated $t\bar{t}$ events, with a mis-tag rate of respectively 8% and 0.3% for jets initiated by charm quarks or light quarks/gluons.

Baseline muon candidates are reconstructed [44] in the region $|\eta| < 2.5$ from MS tracks matching ID tracks. The analysis only considers muons with $p_{\text{T}} > 10$ GeV satisfying a set of requirements on the quality of the tracks defined as `Medium` in Ref. [44]. A longitudinal impact parameter requirement is imposed on the muon track, which must satisfy $|z_0 \sin\theta| < 0.5$ mm. Signal muons are defined as the baseline candidates sufficiently distant from jets (see below) and other leptons, which satisfy further requirements: the transverse impact parameter of the track must be sufficiently small with respect to its uncertainty from the track reconstruction, $|d_0| < 3\sigma(d_0)$, and the candidate must satisfy a track-based isolation criterion. The latter requires the scalar p_{T} sum of nearby ID tracks not to exceed 6% of the muon p_{T}, for selected tracks in a p_{T}-dependent $\Delta R_\eta = \sqrt{(\Delta\eta)^2 + (\Delta\phi)^2}$ cone of maximal radius 0.3 around the muon, excluding its own track, similarly to the isolation variables defined in Ref. [44]; these tracks are required to be associated to the primary vertex to limit sensitivity to pile-up.

Baseline electron candidates are reconstructed [45] from energy depositions in the EM calorimeter matched to an ID track and are required to have $p_{\mathrm{T}} > 10\,\mathrm{GeV}$ and $|\eta| < 2.47$, also excluding the transition region $1.37 < |\eta| < 1.52$ between the barrel and endcap EM calorimeters. They should satisfy the `LooseAndBLayerLLH` identification discriminant similar to that defined in Ref. [45], as well as requirements on the track impact parameters $|z_0 \sin\theta| < 0.5\,\mathrm{mm}$ and $|d_0| < 5\sigma(d_0)$. Signal electrons, which must be distant from jets and other leptons, are required to satisfy the tighter `MediumLLH` identification and `FCTight` isolation requirements similar to those defined in Ref. [45]. The latter are similar to the muon isolation requirement, with maximal cone size of 0.2, but with an additional calorimeter-based isolation requirement using nearby topological clusters instead of tracks. Only signal electrons with $|\eta| < 2.0$ are considered to reduce the rate of electrons with wrongly-reconstructed charge ('charge-flip'); the latter are further rejected by the application of the `ECIDS` discriminant similar to that described in Ref. [45], which exploits further information related to the electron track reconstruction and its compatibility with the primary vertex and the electron cluster.

The missing transverse momentum (and its magnitude $E_{\mathrm{T}}^{\mathrm{miss}}$) is defined as the negative vector sum of the transverse momenta of all identified objects (baseline electrons, photons [46], baseline muons and jets) and an additional soft term. The soft term is constructed from all tracks associated with the primary vertex but not with any physics object. In this way, the $E_{\mathrm{T}}^{\mathrm{miss}}$ is adjusted for the best calibration of the jets and the other identified physics objects listed above, while maintaining approximate pile-up independence in the soft term [47, 48]. Overlaps between objects in the $E_{\mathrm{T}}^{\mathrm{miss}}$ calculation are resolved as described in Ref. [47].

To exclude non-prompt leptons produced inside jets, baseline leptons close to jets are discarded according to the angular distance $\Delta R = \sqrt{(\Delta y)^2 + (\Delta\phi)^2}$ between the two reconstructed objects. A requirement of $\Delta R > \min\{0.4, 0.1 + 9.6\,\mathrm{GeV}/p_{\mathrm{T}}(\ell)\}$ is used.

4 Event selection

Events are selected in the analysis if they contain at least two signal leptons with $p_{\mathrm{T}} > 20\,\mathrm{GeV}$. The leptons must have identical electric charges, unless additional signal leptons with $p_{\mathrm{T}} > 10\,\mathrm{GeV}$ are present in the event.

Data events are recorded via a combination of triggers based on the presence of missing transverse momentum or pairs of leptons [49–51]. For events with $E_{\mathrm{T}}^{\mathrm{miss}} < 250\,\mathrm{GeV}$, only lepton-based triggers without isolation requirements are used, with lepton p_{T} thresholds which varied across the duration of Run 2, up to 24 GeV for triggers requiring two electrons, 22 GeV for the leading-p_{T} muon in triggers requiring two muons, and 17 GeV (respectively 14 GeV) for the electron (muon) in mixed electron+muon triggers. For events with $E_{\mathrm{T}}^{\mathrm{miss}} > 250\,\mathrm{GeV}$, triggers based on $E_{\mathrm{T}}^{\mathrm{miss}}$ are also used. For events that are only accepted by lepton triggers with p_{T} requirements above 20 GeV, the analysis-level lepton p_{T} requirement is raised to be 1 GeV above the trigger threshold. This results in a relative reduction of the total fiducial acceptance by at most 2% for the benchmark signal scenarios of Figure 1. For signal events selected in the SRs presented below, the trigger efficiency is above 95% when R-parity is conserved, and above 93% otherwise. For signal events with $E_{\mathrm{T}}^{\mathrm{miss}} > 250\,\mathrm{GeV}$, the trigger efficiency is above 99%.

Five SRs are built to isolate signatures of hypothetical supersymmetric signal processes from the backgrounds. Their definitions are summarised in Table 1. They rely on the multiplicities of different reconstructed objects such as the number of leptons n_ℓ and their relative electric charges, the number of jets n_j with $p_{\mathrm{T}} > 25$ or 40 GeV, and the number of b-tagged jets n_b with $p_{\mathrm{T}} > 20\,\mathrm{GeV}$. Several kinematic

Table 1: Definition of the signal regions used by the analysis, based on the variables defined in Section 4. The last column provides examples of SUSY processes which may contribute to these signal regions.

SR	n_ℓ	n_b	n_j	$E_{\mathrm{T}}^{\mathrm{miss}}$ [GeV]	m_{eff} [GeV]	$E_{\mathrm{T}}^{\mathrm{miss}}/m_{\mathrm{eff}}$	SUSY
Rpv2L	≥ 2 ($\ell^\pm\ell^\pm$)	≥ 0	≥ 6 ($p_{\mathrm{T}} > 40$ GeV)	–	> 2600	–	$\tilde{g} \to t\tilde{t}_1^*,\ \tilde{t}_1^* \to qq'$ ($\lambda'' \neq 0$) $\tilde{g} \to t\bar{t}\tilde{\chi}_1^0,\ \tilde{\chi}_1^0 \to 3q$ ($\lambda'' \neq 0$) $\tilde{g} \to q\bar{q}\tilde{\chi}_1^0,\ \tilde{\chi}_1^0 \to qq'\ell$ ($\lambda' \neq 0$)
Rpc2L0b	≥ 2 ($\ell^\pm\ell^\pm$)	$= 0$	≥ 6 ($p_{\mathrm{T}} > 40$ GeV)	> 200	> 1000	> 0.2	$\tilde{g} \to q\bar{q}'WZ\tilde{\chi}_1^0$
Rpc2L1b	≥ 2 ($\ell^\pm\ell^\pm$)	≥ 1	≥ 6 ($p_{\mathrm{T}} > 40$ GeV)	–	–	> 0.25	$\tilde{b}_1 \to tW\tilde{\chi}_1^0$
Rpc2L2b	≥ 2 ($\ell^\pm\ell^\pm$)	≥ 2	≥ 6 ($p_{\mathrm{T}} > 25$ GeV)	> 300	> 1400	> 0.14	$\tilde{b}_1 \to tW\tilde{\chi}_1^0$ $\tilde{g} \to t\bar{t}\tilde{\chi}_1^0$
Rpc3LSS1b	≥ 3 ($\ell^\pm\ell^\pm\ell^\pm$)	≥ 1	no cut but veto 81 GeV $< m_{e^\pm e^\pm} <$ 101 GeV			> 0.14	$\tilde{t}_1 \to tW^\pm(W^*)\tilde{\chi}_1^0$

variables are also used: the effective mass m_{eff} consisting of the scalar p_{T} sum of all jets and leptons added to $E_{\mathrm{T}}^{\mathrm{miss}}$, the $E_{\mathrm{T}}^{\mathrm{miss}}$ itself and its ratio to m_{eff}, and the invariant mass of same-sign electron pairs $m_{e^\pm e^\pm}$. The latter helps to reduce the backgrounds featuring a $Z \to e^+e^-$ decay where the charge of one electron is mismeasured. The SR requirements were chosen loosely so as to provide sensitivity to non-excluded regions of the parameter space for the processes illustrated in Figure 1, while preserving sensitivity to other SUSY processes with possibly different final states, as in Table 1.

The SR Rpv2L aims at gluino pair-production in R-parity violating scenarios, hence without any $E_{\mathrm{T}}^{\mathrm{miss}}$ requirement. It is inclusive in terms of b-tagged jets to be sensitive to various decay modes of gluinos leading to final states with leptons and jets, such as the scenario illustrated in Figure 1(d) or the few other examples mentioned in Table 1. In this SR, a tight requirement on the effective mass $m_{\mathrm{eff}} > 2.6$ TeV is used to reduce SM backgrounds.

The SR Rpc2L0b provides sensitivity to R-parity conserving scenarios not involving third-generation squarks, as in Figure 1(c), which are less likely to contain bottom quarks in the final state. A veto on b-tagged jets is imposed in order to reduce SM backgrounds with top quarks. The requirement of a large multiplicity of jets allows a strong reduction in the level of WZ and other multiboson backgrounds.

The SRs Rpc2L1b and Rpc2L2b provide sensitivity to scenarios involving third-generation squarks, such as $\tilde{b}_1 \to t\tilde{\chi}_1^-$ with a subsequent $\tilde{\chi}_1^\pm \to W^\pm\tilde{\chi}_1^0$ decay as in Figure 1(a). Rpc2L2b uses tighter kinematic requirements than Rpc2L1b in order to complement it at low $\tilde{\chi}_1^0$ mass, as well as to provide a good sensitivity to scenarios with heavier superpartners such as pair-produced gluinos decaying via $\tilde{g} \to t\bar{t}\tilde{\chi}_1^0$.

Finally, the SR Rpc3LSS1b probes scenarios with long decay chains but compressed mass spectra leading to final states with softer decay products, such as the $\tilde{t}_1 \to t\tilde{\chi}_2^0 \to tW(W^*)\tilde{\chi}_1^0$ cascade decay shown in Figure 1(b) and proposed in Ref. [52]. This SR selects events with at least three leptons of identical charge, leading to a huge reduction of the expected SM background yields. Loose requirements on the $E_{\mathrm{T}}^{\mathrm{miss}}/m_{\mathrm{eff}}$ ratio and the presence of at least one b-tagged jet, as well as the rejection of events containing any pair of same-sign electrons with $m_{e^\pm e^\pm}$ close to the Z boson mass, help to diminish the residual reducible background to low levels.

A simple cut-and-count analysis is performed in each SR. The number of events in data are reported in Section 7 together with the expected contribution from SM processes and the reducible background, the estimates of which are described in the following sections.

Table 2: List of Monte Carlo event generators and their settings used to predict the contributions from SM processes to the various regions of interest in the analysis. When no reference is provided for the cross-section normalisation, the one computed by the generator is used. The LO and NLO acronyms are defined in Section 5.

Physics process	Event generator	Computation order	Parton shower	Cross-section normalisation	PDF set	Set of tuned parameters
$t\bar{t}W$ [54]	MG5_aMC@NLO 2.3.3 [2]	NLO	Pythia 8.210 [55]	NLO [56]	NNPDF2.3LO [57]	A14 [58]
$t\bar{t}Z/\gamma^*$ [54]	MG5_aMC@NLO 2.3.3 [2]	NLO	Pythia 8.210-212 [55]	NLO [56]	NNPDF2.3LO [57]	A14 [58]
$t\bar{t}WW$	MG5_aMC@NLO 2.2.2 [2]	LO	Pythia 8.186 [59]	NLO [2]	NNPDF2.3LO [57]	A14 [58]
$t\bar{t}WZ$	MG5_aMC@NLO 2.2.2 [2]	LO	Pythia 8.212 [55]	NLO [2]	NNPDF2.3LO [57]	A14 [58]
tWZ, tZ	MG5_aMC@NLO 2.3.3 [2]	LO	Pythia 8.212 [55]	NLO [2]	NNPDF2.3LO [57]	A14 [58]
$t\bar{t}H$ [54]	Powheg 2 [60]	NLO	Pythia 8.230 [55]	NLO [56]	NNPDF2.3LO [57]	A14 [58]
$3t, 4t$	MG5_aMC@NLO 2.2.2 [2]	LO	Pythia 8.186 [59]	NLO [2]	NNPDF2.3LO [57]	A14 [58]
$pp \to 4\ell, 3\ell\nu$ [61]	Sherpa 2.2.2 [62]	NLO (0-1j) + LO (2-3j)	Sherpa	NLO	NNPDF3.0NNLO [63]	Sherpa
$gg \to 4\ell$ [61]	Sherpa 2.2.2 [62]	LO (0-1j)	Sherpa	NLO	NNPDF3.0 NNLO [63]	Sherpa
$pp \to (2\ell 2\nu/3\ell\nu/4\ell)jj$ [53, 61]	Sherpa 2.2.2 [62]	LO	Sherpa	LO	NNPDF3.0NNLO [63]	Sherpa
WH, ZH	Pythia 8.186 [59]	LO	Pythia	LO	NNPDF2.3LO [57]	A14 [58]
$VVV^{(*)}$	Sherpa 2.2.1 [62]	LO (0-1j)	Sherpa	LO	NNPDF3.0NNLO [63]	Sherpa
$VVVjj$ [61]	Sherpa 2.2.2 [62]	LO (0-1j)	Sherpa	LO	NNPDF3.0NNLO [63]	Sherpa

5 Standard Model backgrounds

Major contributions from SM processes to the SRs arise from WZ+jets (with minor contributions from ZZ and $W^{\pm}W^{\pm}jj$[3]), $t\bar{t}W$ and $t\bar{t}Z/\gamma^*$. The summed contributions of other processes involving associated production of a larger number of top quarks or massive bosons, with smaller production cross-sections, can also amount to significant fractions of the expected SR event yields. SRs with at least one b-tagged jet are dominated by processes involving top quarks, while multiboson processes dominate in regions vetoing b-jets. In the case of the `Rpc3LSS1b` SR, only processes such as WZZ, ZZZ, $t\bar{t}WZ$ and $VH/t\bar{t}H$ where the Higgs boson H decays via $H \to 4\ell$ are genuine sources of events with three same-sign prompt leptons.

The contributions of these processes to the SRs are evaluated with Monte Carlo simulations to determine the fiducial acceptance of the various regions as well as the efficiencies of the detector and reconstruction software. Table 2 provides a complete list of the relevant processes considered in this analysis, the event generators used for the predictions and their settings. For the processes with largest production cross-sections, the scattering amplitudes evaluated for the event generation rely on terms up to the next-to-leading order (NLO) in the perturbative expansion, while for other processes only leading-order (LO) terms are accounted for. For most processes, the generated events are normalised to the inclusive cross-section computed with NLO accuracy, either taken from the references indicated in Table 2, or directly from the generator. The generated events for the $t\bar{t}Z$, tZ, $t\bar{W}Z$, VZ and VVZ processes include matrix elements for non-resonant $Z/\gamma^* \to \ell\ell$ contributions; the same is true for non-resonant $W^* \to \ell\nu$ in events from VV and VVV processes. For the `Rpc3LSS1b` SR, only contributions from processes with three same-sign prompt leptons are evaluated with Monte Carlo simulations, while the others (VV, $t\bar{t}V\ldots$) are accounted for by the reducible background estimate described in Section 6.

The generated events were processed through a detailed simulation of the ATLAS detector [64] based on Geant4 [65]. To simulate the effects of additional pp collisions in the same and nearby bunch crossings, inelastic interactions were generated using the soft strong-interaction processes of Pythia 8.1.86 [55] with a set of tuned parameters referred to as the A3 tune [66] and the NNPDF23LO parton distribution function (PDF) set [57]. These inelastic interactions were overlaid onto the simulated hard-scatter event

[3] This process corresponds to the production of two same-sign W bosons [53] which at the lowest order of the perturbative expansion are accompanied by two forward jets.

and reweighted to match the pile-up conditions observed in the data. In all Monte Carlo samples, except those produced by the Sherpa event generator, the EvtGen 1.2.0 program [67] was used to model the properties of bottom and charm hadron decays. The predicted event yields are normalised to the reference cross-sections available in the literature, or in the case of less common processes directly to the cross-section computed by the generator employed for the prediction.

Simulated events are weighted by scale factors to account for the mismodelling of inefficiencies in the reconstruction of leptons and the application of identification and isolation requirements, in the lepton-based trigger chains, and in the application of the pile-up rejection (JVT) and b-tagging requirements for both jets that do or do not contain genuine b-flavoured hadrons.

Various sources of systematic uncertainties in the predicted event yields are accounted for. Experimental sources, evaluated for all processes, include uncertainties in the calibration of momentum scale and resolution for jets, leptons and the soft term of the missing transverse momentum, as well as uncertainties in the various scale factors mentioned above, in the measured integrated luminosity, and in the distribution of the number of parasitic interactions per event.

Uncertainties in the theoretical modelling of each process are also considered. Uncertainties in the inclusive production cross-sections of $t\bar{t}W$, $t\bar{t}Z$ and $t\bar{t}H$ are taken respectively as 12%, 13% and 8% [56], while a 6% uncertainty is retained for VV processes [61]. The impact of the choice of factorisation and renormalisation scales on the estimated fiducial acceptance and reconstruction efficiencies of the SRs is assessed by considering the alternative event weights provided by the generators that correspond to up/down variations of these scales (see e.g. appendix B.3 in [2]). The impact of PDF uncertainties is also taken into account by following the prescription in Ref. [68] using the sets of eigenvectors provided for each PDF [57, 63].

For $t\bar{t}V$ and $t\bar{t}H$ processes, the modelling of initial and final state radiations by the parton shower algorithm is assessed by comparing five related variations of the Pythia 8 A14 event tune [58]. For $t\bar{t}W$ the modelling of extra jets is further compared to the prediction of the Sherpa 2.2.2 generator including LO matrix elements with two extra final state partons; the difference is found to be smaller than the tune-based parton shower uncertainties.

For VV processes, the impact of the choice of resummation scale (QSF) and CKKW matching scale [69] is also evaluated by comparing the nominal prediction to alternatives obtained with variations of these scales. In addition, the modelling of high jet multiplicities is probed by switching between different parton shower recoil schemes implemented in the Sherpa generator [70, 71].

Overall, modelling uncertainties in the SRs where these processes have sizeable contributions are 35–45% for $t\bar{t}W$, 25–45% for $t\bar{t}Z$, and 40–45% for WZ. For all other processes, uncertainties of 50% are considered. The latter numbers are believed to be conservative as these processes produce larger number of jets at the first order of the perturbative expansion, rendering them less sensitive to e.g. parton shower modelling uncertainties. Modelling uncertainties are further assumed to be uncorrelated between processes shown in different categories in the tables and figures.

Three validation regions (VRs) enriched respectively in WZ+jets (`VRWZ4j`, `VRWZ5j`) and $t\bar{t}V$ (`VRttV`) allow checking the accuracy of the modelling of these processes by comparing event yields predicted in a signal-free environment to data. The definitions of these regions are provided in Table 3, and particularly aim at decreasing the level of reducible background. Requirements are set on some of the variables defined in Section 4. The presence of a pair of same-flavour opposite-sign (SFOS) leptons is required in `VRWZ4j` and `VRWZ5j`, and its invariant mass m_{SFOS} must be close to m_Z. A minimum angular separation between the leading-p_{T} lepton and the jets ($\Delta R(\ell_1, j)$) is required in `VRttV`, together with a requirement on the

Table 3: Event selection defining the three validation regions enriched in WZ+jets and $t\bar{t}V$ SM processes, based on the variables defined in Section 5.

	n_ℓ	n_b	n_j	m_{eff} [GeV]	Other requirements
VRWZ4j	= 3,	= 0	≥ 4 (p_{T} >25 GeV)	> 600	81 GeV < m_{SFOS} < 101 GeV, $E_{\text{T}}^{\text{miss}} > 50$ GeV,
VRWZ5j	= 1 SFOS pair	= 0	≥ 5 ($p_{\text{T}} > 25$ GeV)	> 400	no fourth baseline lepton
VRttV	≥ 2 ($\ell^\pm\ell^\pm$)	≥ 1	≥ 3 ($p_{\text{T}} > 40$ GeV)	> 600	$p_{\text{T}} > 30$ GeV for the same-sign leptons, $\sum p_{\text{T}}^b > 0.4 \sum p_{\text{T}}^j$, $E_{\text{T}}^{\text{miss}} > 0.1 m_{\text{eff}}$, $\Delta R_\eta(\ell_1, j) > 1.1$
All VRs	$m_{\text{eff}} < 1.5$ TeV, $E_{\text{T}}^{\text{miss}} < 250$ GeV; veto Rpc2L1b, Rpc2L2b, Rpc2L0b and Rpv2L signal regions.				

Table 4: Number of data events compared to the expected contributions from relevant SM processes and the reducible background, in the three VRs enriched in WZ+jets and $t\bar{t}V$ processes. The displayed numbers include all sources of statistical and systematic uncertainties; since some of the latter might be correlated between different processes, the numbers do not necessarily add up in quadrature to the uncertainty in the total expected background. The uncertainties shown in this table are symmetrised. Selections with three leptons are not affected by the charge-flip electron background, therefore such contributions are denoted by –.

	VRttV	VRWZ4j	VRWZ5j
Observed	127	355	190
Total background	106 ± 17	400 ± 110	215 ± 60
$t\bar{t}W$	25.8 ± 5.5	0.40 ± 0.14	0.3 ± 0.1
$t\bar{t}Z$	34.4 ± 8.0	37.2 ± 8.7	27.3 ± 7.2
WZ	5.8 ± 2.3	310 ± 110	153 ± 57
ZZ, $W^\pm W^\pm$, VH, VVV	1.25 ± 0.44	24.4 ± 5.7	14.1 ± 3.9
$t(W)Z$, $t\bar{t}H$, $t\bar{t}VV$, $3t$, $4t$	17.6 ± 5.5	11.2 ± 5.3	6.6 ± 3.1
Fake/non-prompt	14 ± 10	15.4 ± 9.9	13.7 ± 6.7
Charge-flip	7.1 ± 5.7	–	–

ratio between the scalar p_{T} sum over all b-tagged jets and the sum over all jets. For all VRs, events belonging to any SR (but Rpc3LSS1b) are vetoed. Upper cuts on $E_{\text{T}}^{\text{miss}}$ and m_{eff} are also applied to minimise contributions from the benchmark SUSY scenarios of Figure 1. Modelling uncertainties are evaluated with the same procedure as described above for the SRs, and lead to uncertainties around 20% for $t\bar{t}V$ and 35% for WZ processes.

The number of events observed in the three VRs and the corresponding predictions for SM processes are shown in Table 4, including the reducible background described in the next section, accounting for the systematic and statistical uncertainties. The predicted event yields in all VRs are consistent with the data. In the VRWZ4j and VRWZ5j regions, where the differences can be up to 20%, the large systematic uncertainties include contributions both from theoretical modelling and experimental sources (dominated by the jet energy scale) due to the large required number of jets.

Other potential sources of same-sign leptons in the SRs are not accounted for, as they were estimated to be negligible. These include simultaneous production of massive bosons or top quarks via either double parton scattering (DPS) or pile-up interactions. Simple estimates of the inclusive production cross-sections

were performed for several processes. For DPS the approach from Ref. [72] was used, relying on the DPS effective cross-section σ_{eff} [73]. For pile-up interactions, the estimate was based on the longitudinal density of reconstructed vertices [74], as the impact parameter requirements in the selection of the leptons strongly affect the yields of such processes. The largest contribution of these sources, relatively to the corresponding SM process, corresponds to a fraction of $W^{\pm}W^{\pm}$ production, which has indeed been highlighted [75] as a sensitive process for DPS measurements. But this process is in itself a minor background for this analysis.

Another source, notably highlighted in Ref. [76], is the production of additional pairs of leptons in radiative top quark decays, $t \to \ell\nu b\ell\ell$ or $t \to qqb\ell\ell$, which are not included in the generator matrix elements for the $t\bar{t}Z$ process. These contributions were studied by running the Photos++ QED shower program [77] on the tree-level decay products of top quarks generated with MadGraph 2.6 or Pythia 8. The fraction of events in which an additional lepton is produced drops sharply with the p_{T} requirement for that lepton; for a $p_{\text{T}} > 10\,\text{GeV}$ threshold[4] this fraction was found to be $\sim 0.2\%$, a similar order of magnitude as that quoted in Ref. [77]. An additional isolation requirement similar to that used in the analysis reduces this rate by a factor of three. This represents less than 2% (4%) of the inclusive contribution from $t\bar{t}V$ processes for final states with same-sign (three) leptons; furthermore the smaller reconstruction and identification efficiencies for low-p_{T} leptons should further reduce the radiative top quark decay contribution with respect to $t\bar{t}V$ processes. The expected contribution to the SRs is therefore small enough to be neglected as well.

6 Reducible background

Other SM processes that do not lead to genuine production of same-sign prompt leptons, such as $t\bar{t}$ processes and to a much lesser extent production of W/Z+jets or single top quarks, might contaminate the SRs via misidentification of the reconstructed objects.

The first source consists of 'charge-flip' electrons, where the charge of a prompt electron is mismeasured due to the emission of a bremsstrahlung photon which through interaction with detector material converts into a pair of secondary electron tracks, one of which happens to better match the position of the calorimeter cluster than the original electron track, and has the opposite charge with respect to the electron. Thanks to the application of the `ECIDS` discriminant for signal electrons, charge-flip electrons are only a minor background to the SRs. Muon charge-flip is negligible in the p_{T} range relevant to this analysis.

Backgrounds with charge-flip electrons are estimated by selecting data events with two opposite-sign leptons, and weighting them by the probability of one electron charge to be mismeasured. This offers a large improvement in statistical accuracy over relying directly on the simulation for these backgrounds, as well as the elimination of associated experimental and theory uncertainties. The charge-flip probabilities are measured in simulated $t\bar{t}$ events, as a function of p_{T} and $|\eta|$. They are corrected by scale factors corresponding to the ratio of probabilities measured in data and simulation from the reconstructed charges of electrons produced in $Z \to e^{+}e^{-}$ decays and selected with a 'tag and probe' method [45]. The probabilities reach $O(0.1\%)$ at $p_{\text{T}} = 100\,\text{GeV}$ for central electrons ($|\eta| < 1.4$), and are about fives times larger at higher $|\eta|$ due to the larger amount of material traversed by electrons. Systematic uncertainties are assessed by propagating the measurement uncertainties, leading to a 70–90% uncertainty in the predicted SR yields.

The data weighting method described above neglects the differences in momentum scale and resolution between standard and charge-flip electrons. This approximation was validated by recomputing the expected

[4] Dilepton $t\bar{t}$ events with an extra $p_{\text{T}} > 10\,\text{GeV}$ lepton satisfy the lepton selection requirements of this analysis.

SR yields after reducing the p_{T} of the electron with largest $|\eta|$ by 5 GeV in all weighted data events, which was found to have a negligible impact on the results. For the `Rpc3LSS1b` SR, the method is adapted by simply selecting data events with three or more leptons, which are weighted by the probability of one or more electron charges to be mismeasured such that the resulting event contains three same-sign leptons.

Another, more important, source of reducible background includes fake or non-prompt leptons, referred to in the following as 'F/NP' leptons. They may originate from electroweak-mediated decays of hadrons (in particular b- and c-flavoured hadrons in decays of top quarks and weak bosons), single pions stopped in the EM calorimeter and faking electron signatures, in-flight decays of kaons into muons, or conversion of photons from various origins into pairs of electrons caused by interactions with the beam pipe or detector material. Lepton candidates reconstructed from these different sources however share the properties of being generally not well isolated, and are mostly rejected by the lepton identification criteria and impact parameter requirements. Therefore, all sources of background with F/NP leptons are estimated altogether with a common method exploiting these properties.

Sources of F/NP leptons in the SRs are mostly semi- or dilepton $t\bar{t}$ processes. To estimate their contributions to the SRs, a matrix method similar to that described in Ref. [78] is used. It relies on data events selected with identical criteria as the region of interest, but with a loosened lepton selection corresponding to the baseline leptons defined in Section 3 after the overlap removal procedure with a few extra adjustments: muons are required to satisfy a loosened transverse impact parameter requirement $|d_0| < 7\sigma(d_0)$, and electrons should both be within $|\eta| < 2.0$ and satisfy the `ECIDS` requirement against charge-flip. These adjustments allow alignment with the fiducial acceptance of signal leptons, and eliminate irrelevant sources of reconstructed leptons. The matrix method, for the simplest situation where selected events contain a single lepton, relies on the following asymptotic equality for the observed proportion of events $\mathcal{S}$ where the lepton satisfies the signal lepton requirements:

$$\mathcal{S} = \varepsilon\,(1 - \mathcal{F}) + \zeta\mathcal{F} \tag{1}$$

where $\mathcal{F}$ is the unknown proportion of events with a F/NP lepton, while ε and ζ are respectively the probabilities for a prompt and F/NP lepton to satisfy the signal lepton requirements. If ε and ζ are known, this equation can be used to determine $\mathcal{F}$ and thus the number of events with a F/NP lepton in the region of interest. The approach can be generalised to events with arbitrary numbers of leptons, as well as the more realistic situation where ε and ζ depend on the flavour and kinematic properties of the leptons.

The probabilities ε are obtained directly from the $t\bar{t}$ simulation, as a function of p_{T} and $|\eta|$, accounting for the various lepton-related scale factors mentioned in Section 5. They are typically above 82% and 89% for electrons and muons, respectively, in simulated $t\bar{t}V$ events. As ε might be smaller in data events coming from signal scenarios with busy environments, such as leptonically-decaying boosted top quarks, dedicated uncertainties are taken into account as a function of p_{T} and the proximity to the closest jet, which can be as large as 30% for $\Delta R < 0.4$.

The probabilities ζ are measured in regions of the data enriched in F/NP leptons produced by $t\bar{t}$ processes, defined by selecting events with two same-sign or three leptons, at least one b-tagged jet, $E_{\mathrm{T}}^{\mathrm{miss}} > 30$ GeV and $\geq$ 2–3 jets; upper cuts on $E_{\mathrm{T}}^{\mathrm{miss}}$ and m_{eff} avoid contamination from supersymmetric processes. They are measured as a function of p_{T}, separately for events with exactly one or exactly two b-tagged jets, as the proportion of non-prompt leptons from b-flavoured hadron decays is much smaller in the latter case with respect to events with 0 or 1 b-tagged jet. They are also measured separately for electrons that were or were not used to accept the event via a lepton-based trigger, as the requirements for electrons reconstructed

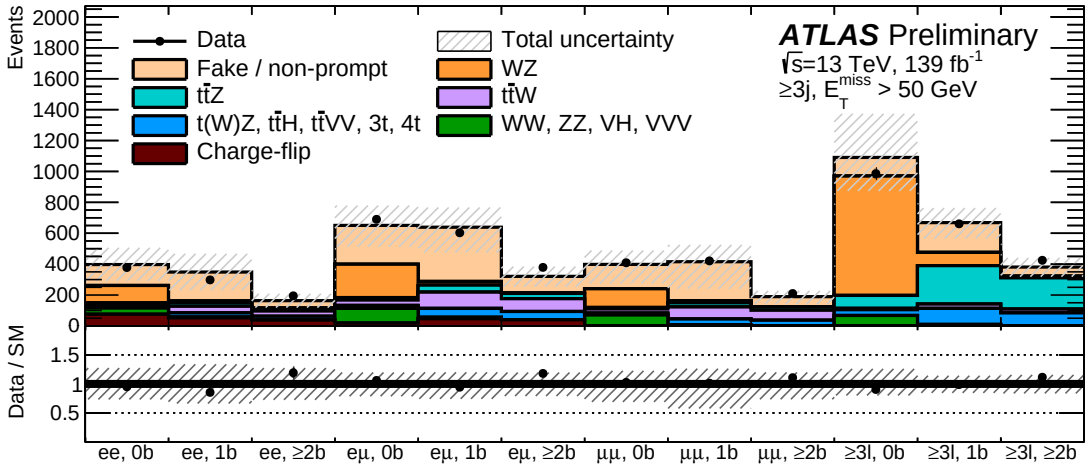

Figure 2: Data event yields compared to the expected contributions from relevant SM processes and the reducible background, after a loose preselection requiring events with same-sign leptons, $E_{\mathrm{T}}^{\mathrm{miss}} > 50\,\mathrm{GeV}$ and at least three jets with $p_{\mathrm{T}} > 40\,\mathrm{GeV}$. The observed and predicted event yields are classified as a function of the number and flavour of the leptons, as well as the number of b-tagged jets. The uncertainties, shown with hashed bands, include the total uncertainties in the reducible background, as well as the modelling and statistical uncertainties for the Monte Carlo simulations.

online differ from those reconstructed offline. The measured probabilities are $\sim 10\%$ for both electrons and muons up to $p_{\mathrm{T}} \sim 35\,\mathrm{GeV}$, and increase up to 20% and 35% for electrons and muons with $p_{\mathrm{T}} > 60\,\mathrm{GeV}$. They can be up to twice as large in events with two b-tagged jets.

Systematic uncertainties in the measured ζ probabilities account for variations in the relative contributions of different sources of F/NP leptons or in the environment, and they are assessed in simulated $t\bar{t}$ events. For electrons the latter amount to a 30% extra uncertainty. For muons the probabilities become smaller in events with a larger amount of activity, where non-prompt muons tend to be less well-isolated. This leads to extra uncertainties from 30% to 80% for $p_{\mathrm{T}} > 50\,\mathrm{GeV}$, as this effect is not accounted for with the simple p_{T}-based parameterisation used for ζ.

Events with charge-flip electrons may bias the matrix method prediction, as the probability for such electrons to satisfy signal lepton requirements differ from both standard and F/NP electrons. For that reason, estimated charge-flip contributions are subtracted from the data event yields when the method is applied.

The data-driven methods employed to estimate the reducible background are validated by comparing the event yields in data to the combined predictions for these backgrounds, added to Monte Carlo predictions for SM processes as described in Section 5. Figure 2 shows such a comparison for a loose event preselection requiring same-sign leptons, $E_{\mathrm{T}}^{\mathrm{miss}} > 50\,\mathrm{GeV}$ and at least three jets with $p_{\mathrm{T}} > 40\,\mathrm{GeV}$, binned in the different lepton flavour, and b-tag multiplicity combinations. Simulation studies show that sources of reducible background for such a preselection are also dominated by $t\bar{t}$ processes, as in the SRs. In all bins, the observed and predicted event yields agree within uncertainties. Figure 3 presents the distributions of $E_{\mathrm{T}}^{\mathrm{miss}}$ and the number of jets, for which a good agreement is also observed between data and predictions.

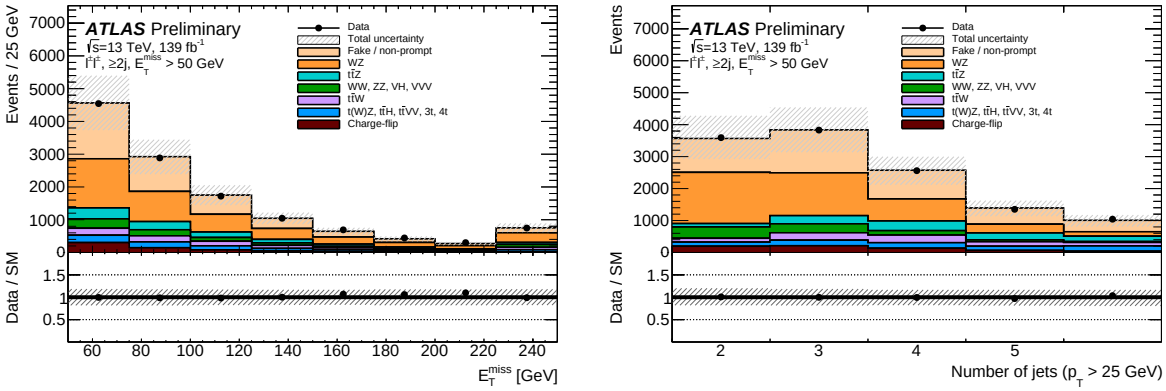

Figure 3: Distributions of (left) $E_{\mathrm{T}}^{\mathrm{miss}}$ and (right) the number of jets with $p_{\mathrm{T}} > 25\,\mathrm{GeV}$, after a loose preselection requiring events with same-sign leptons, $E_{\mathrm{T}}^{\mathrm{miss}} > 50\,\mathrm{GeV}$ and at least two jets with $p_{\mathrm{T}} > 40\,\mathrm{GeV}$. The uncertainties, shown with hashed bands, include the total uncertainties in the reducible background, as well as the modelling and statistical uncertainty for the Monte Carlo simulations. The last bin is inclusive.

As $t\bar{t}$ processes with F/NP leptons account for a major background to this analysis, the estimated SR yields obtained with the matrix method are cross-checked against an alternative method. In the latter, a control region CR is built for each SR by relaxing some of the $E_{\mathrm{T}}^{\mathrm{miss}}$ or m_{eff} requirements. Another set of regions SR′ and CR′ is built with identical criteria but using events where a single lepton is selected instead of the same-sign pair, as well as an additional object (jet, b-tagged jet, photon) that might be a source of F/NP leptons. A 'transfer factor' is built as the ratio between the number of data events in SR′ and CR′. The transfer factor is then multiplied by the number of same-sign leptons events in the CR to obtain an estimate of the F/NP lepton background yield in the SR. The estimated contributions to the CR from SM processes with same-sign prompt leptons are subtracted, as well as the charge-flip background. The CR is chosen such that the kinematic properties of the additional object are similar in that region and the SR. Variations of the nature of the additional object lead to differences in the transfer factor, which is treated as a source of systematic uncertainty. The estimated F/NP lepton background yields in the five SRs obtained with this alternative method are consistent with the matrix method prediction within uncertainties.

7 Results

The event yields in data in the five SRs, and the corresponding estimates for SM processes and the reducible background, are shown in Figure 4 and with more details in Table 5. No significant excess over the expected yields is observed in any of the SRs. The SRs `Rpc2L1b` and `Rpc2L2b` overlap by approximately 15% in terms of expected yields from SM processes, and two data events satisfy the requirements for both regions. Among SM processes with smaller cross-sections, the largest contributions originate from $t\bar{H}$ (in `Rpc2L1b`) and $4t$ (in `Rpc2L2b`, `Rpv2L`). The distributions of $E_{\mathrm{T}}^{\mathrm{miss}}$, m_{eff} or the $E_{\mathrm{T}}^{\mathrm{miss}}/m_{\mathrm{eff}}$ ratio are shown near the SRs in Figure 5 for four of the SRs by relaxing the SR requirement for the displayed variable. When $E_{\mathrm{T}}^{\mathrm{miss}}$ is relaxed (`Rpc2L0b`, `Rpc2L2b`), the m_{eff} requirement is also loosened by the difference between the actual $E_{\mathrm{T}}^{\mathrm{miss}}$ and the minimum $E_{\mathrm{T}}^{\mathrm{miss}}$ required in the SR, to avoid selecting harder jets or leptons in the low-$E_{\mathrm{T}}^{\mathrm{miss}}$ region. The $E_{\mathrm{T}}^{\mathrm{miss}}/m_{\mathrm{eff}}$ requirement is loosened similarly. For `Rpc2L0b`, the small number of events in the low-$E_{\mathrm{T}}^{\mathrm{miss}}$ region, compared to the SR, is due to the combined effects of the m_{eff} and $E_{\mathrm{T}}^{\mathrm{miss}}/m_{\mathrm{eff}}$

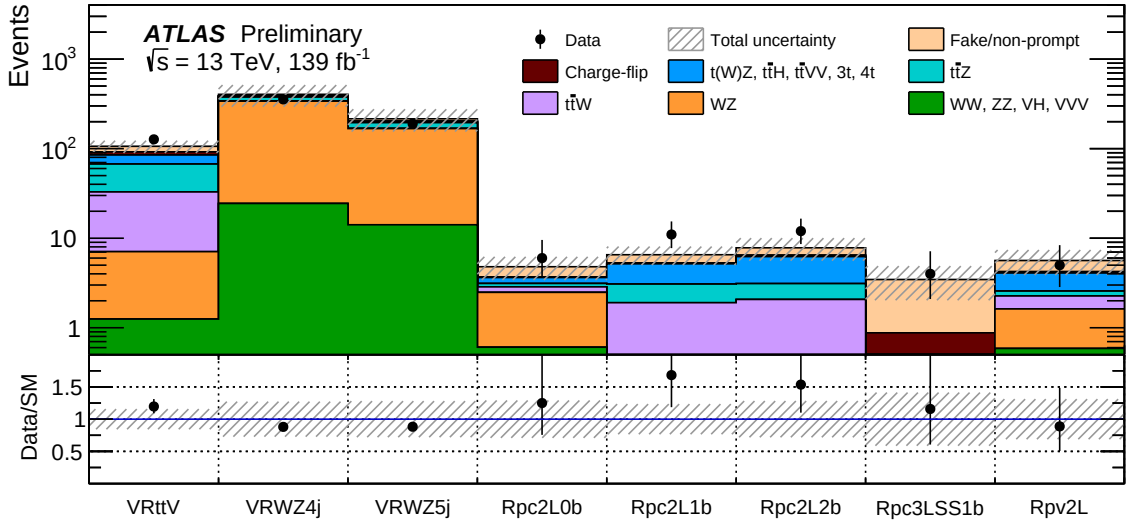

Figure 4: Data event yields compared to the expected contributions from relevant SM processes and the reducible background, in the three VRs and the five SRs. The total uncertainties in the expected event yields are shown as the hashed bands.

Table 5: Number of data events and expected contributions from SM processes and the reducible background to the five SRs. The displayed numbers include all sources of statistical and systematic uncertainties; since some of the latter might be correlated between different processes, the numbers do not necessarily add up in quadrature to the uncertainty in the total expected background. The uncertainties shown in this table are symmetrised. The WZ and $t\bar{t}V$ processes cannot genuinely result in final states with three same-sign leptons, therefore their contributions to the `Rpc3LSS1b` signal region are denoted by –. Contributions to `Rpc3LSS1b` only include those from processes with genuine three-same-sign leptons final states, such as $t\bar{t}WZ$ or WZZ.

	`Rpc2L0b`	`Rpc2L1b`	`Rpc2L2b`	`Rpc3LSS1b`	`Rpv2L`
Observed	6	11	12	4	5
Total SM background	4.8 ± 1.4	6.5 ± 1.5	7.8 ± 2.2	3.5 ± 1.4	5.6 ± 1.8
$t\bar{t}W$	0.38 ± 0.21	1.56 ± 0.61	1.81 ± 0.67	–	0.64 ± 0.29
$t\bar{t}Z$	0.26 ± 0.10	1.17 ± 0.42	1.04 ± 0.31	–	0.30 ± 0.16
WZ	1.88 ± 0.80	0.29 ± 0.13	0.21 ± 0.10	–	1.03 ± 0.46
ZZ, $W^{\pm}W^{\pm}$, VH, VVV	0.61 ± 0.19	0.05 ± 0.03	0.05 ± 0.02	< 0.02	0.59 ± 0.17
$t(W)Z$, $t\bar{t}H$, $t\bar{t}VV$, $3t$, $4t$	0.51 ± 0.21	2.10 ± 0.75	3.2 ± 1.3	0.36 ± 0.06	1.52 ± 0.70
Fake/non-prompt	1.1 ± 1.0	1.3 ± 1.0	1.4 ± 1.5	2.6 ± 1.4	1.4 ± 1.5
Charge-flip	0.05 ± 0.04	0.11 ± 0.11	0.22 ± 0.22	0.52 ± 0.39	0.14 ± 0.14

requirements, preventing high-m_{eff} events from being selected.

Figure 6 presents a summary of the contributions from different sources of systematic uncertainty to the total uncertainties in the predicted total background yields. These range from 23 to 41%, and are always smaller than the statistical uncertainties in the observed event yields. While many sources of uncertainties are asymmetric, and are treated as such in the statistical analysis of the results, the tables and figures display symmetrised uncertainties for simplicity.

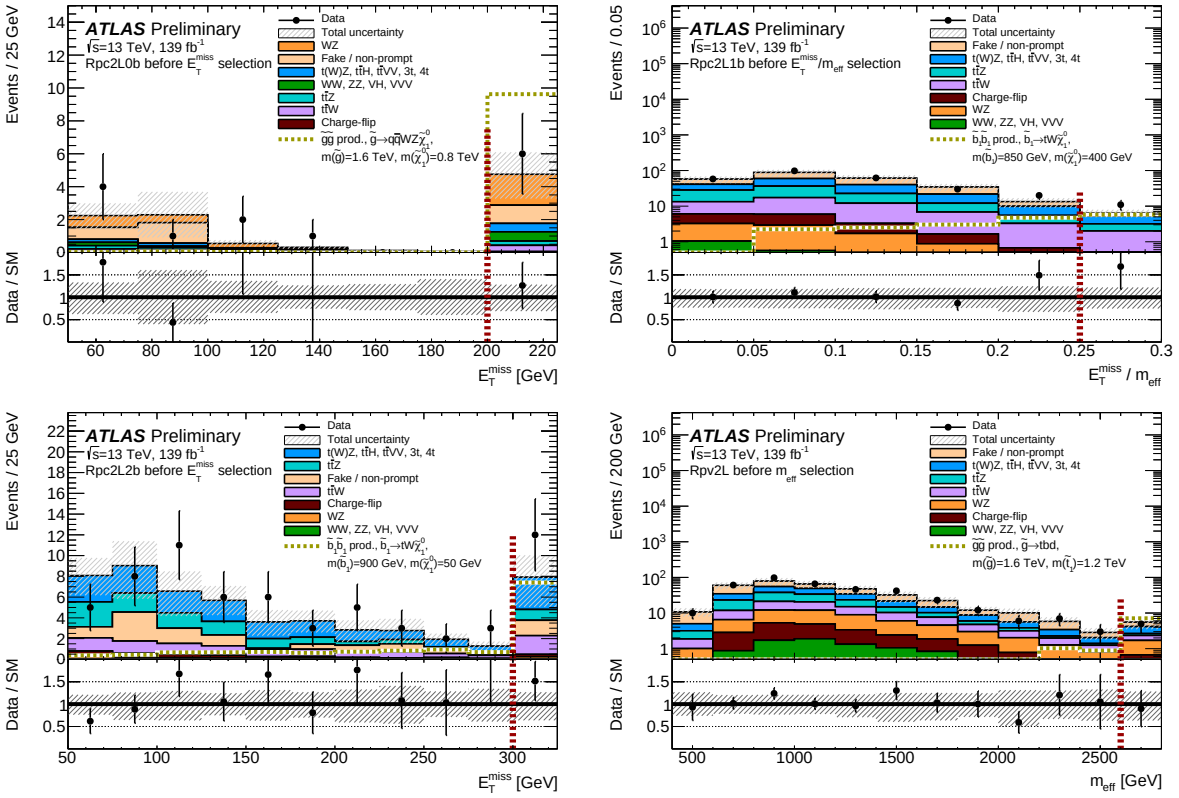

Figure 5: Distributions of $E_{\mathrm{T}}^{\mathrm{miss}}$, m_{eff} or the $E_{\mathrm{T}}^{\mathrm{miss}}/m_{\mathrm{eff}}$ ratio near the SRs (top left) `Rpc2L0b`, (top right) `Rpc2L1b`, (bottom left) `Rpc2L2b` and (bottom right) `Rpv2L`. The total uncertainties in the expected event yields are shown as the hashed bands. The last bin, isolated by a vertical red dashed line, is inclusive and corresponds to the SR.

Upper limits at 95% confidence level on possible BSM contributions to the SRs are computed with the HistFitter framework [79], relying on a profile-likelihood-ratio test [80] and following the $\mathrm{CL_s}$ prescription [81]. The hypothesis tests are performed for each of the SRs independently. The likelihood is built as the product of a Poisson probability distribution describing the observed number of events in the SR and the probability distributions of the nuisance parameters encoding the systematic uncertainties. The latter are either Gaussian distributions for most sources or Poisson distributions for statistical uncertainties arising from limited number of preselected or opposite-sign data events in the estimation of the reducible background, or limited number of simulated events. Correlations of a given nuisance parameter between the backgrounds and the signal are taken into account when relevant.

Table 6 presents 95% confidence level upper limits on the number of BSM events S^{95} that may contribute to the SRs. Normalising these by the integrated luminosity L of the data sample, they can be interpreted as upper limits on the visible BSM cross-section (σ_{vis}), defined as $\sigma_{\mathrm{vis}} = \sigma_{\mathrm{prod}} \times \mathcal{A} \times \epsilon = S^{95}/L$, where σ_{prod} is the production cross-section of an arbitrary BSM signal process, and $\mathcal{A}$ and ϵ are the corresponding fiducial acceptance and reconstruction efficiency for the relevant SR. These limits are computed with asymptotic approximations of the probability distributions of the test statistics under the different hypotheses [80]. They were checked to be within 10% of an alternative computation based on pseudoexperiments. The compatibility of the observations with the SM-only hypothesis is quantified by the p-values displayed in Table 6; the smallest, for `Rpc2L1b`, corresponds to about 1.3 standard deviations.

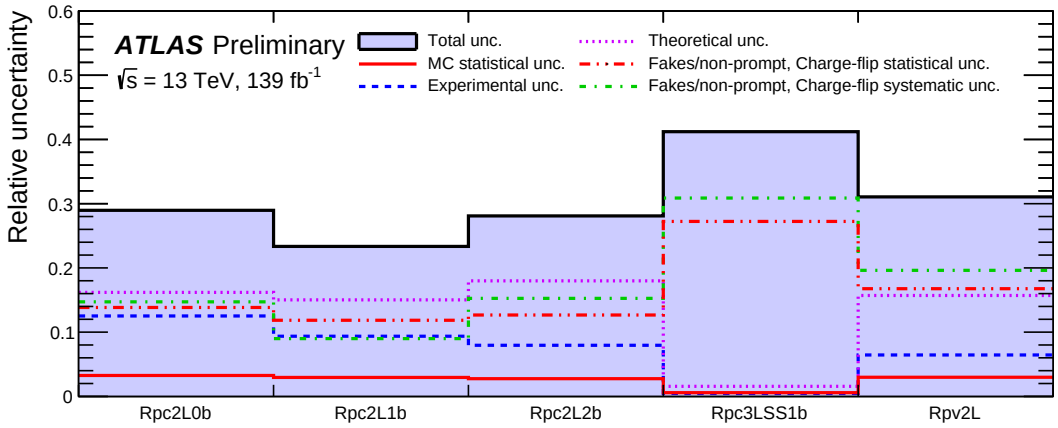

Figure 6: Contributions of different categories of uncertainties relatively to the expected background yields in the five SRs. The 'statistical' uncertainties originate from the limited number of preselected or opposite-sign data events used respectively in the matrix method and the charge-flip electron background estimate, as well as the effect of limited numbers of simulated events for SM processes.

Table 6: Computed 95% confidence level upper limits on the numbers of BSM events S^{95}, as well as the $\pm 1\sigma$ expected fluctuations around the mean expected limit. These are also translated into upper limits on the visible cross-section σ_{vis}. The p-values $p(s = 0)$ give the probabilities to observe a deviation from the predicted background at least as large as that in the data. They are capped at 0.5.

Signal region	σ_{vis} [fb]	S^{95}_{obs}	S^{95}_{exp}	$p(s = 0)$
Rpc2L0b	0.05	7.5	$6.4^{+3.2}_{-2.0}$	0.33
Rpc2L1b	0.08	11.6	$7.3^{+3.6}_{-2.3}$	0.09
Rpc2L2b	0.09	12.4	$8.7^{+4.0}_{-2.7}$	0.14
Rpc3LSS1b	0.04	6.2	$5.7^{+2.9}_{-1.8}$	0.41
Rpv2L	0.05	6.6	$7.0^{+3.2}_{-2.1}$	0.50

8 Exclusion limits on SUSY scenarios

Exclusion limits are computed for the masses of superpartners involved in the benchmark SUSY signal scenarios shown in Figure 1, with the same statistical tools as those described in Section 7. The limits are obtained in the context of simplified models [82–84] assuming a single production process with 100% branching ratio into the chosen decay mode, and where superpartners not involved in the process are treated as decoupled. All superpartners are assumed here to decay promptly. The expected signal contributions to the SRs are estimated from simulated Monte Carlo samples produced with the MadGraph5_aMC@NLO 2.2.1 generator using LO matrix elements for the signal process with up to two extra partons. Parton shower, hadronisation and modelling of the underlying event were performed using the Pythia 8.230 generator [55] with the A14 tune [58], using the CKKW-L matching prescription [85] with a matching scale set to one quarter of the pair-produced superpartner mass. The samples were processed through a fast simulation of the ATLAS detector using a parameterisation of the calorimeter response and Geant4 for the ID and MS [64, 86]. They are normalised to the 'NNLO$_{\text{approx}}$+NNLL' reference cross-sections [27], which combine near-threshold approximate next-to-next-to-leading-order corrections [87] to the NLO cross-section, with the resummation of soft gluon divergences at next-to-next-to-leading logarithmic accuracy [27]. Corresponding uncertainties are taken from envelopes of cross-section predictions using different PDF sets and factorisation and renormalisation scales, as described in Ref. [68]. They range from 12% to 20% for gluino masses from 1 to 2 TeV, and from 7% to 11% for top or bottom squark masses from 400 GeV to 1 TeV.

Exclusion limits on the masses of gluinos are shown in Figure 7. The limits in Figure 7(a) are set for pair-production of gluinos in an R-parity conserving scenario (Figure 1(c)) with decoupled squarks and gluinos decaying in two steps with intermediate $\tilde{\chi}_1^\pm$ and $\tilde{\chi}_2^0$ into jets, weak bosons and the LSP $\tilde{\chi}_1^0$. The $\tilde{\chi}_1^\pm$ mass is assumed to be $0.5 \times \{m(\tilde{g}) + m(\tilde{\chi}_1^0)\}$, while the $\tilde{\chi}_2^0$ mass is similarly $0.5 \times \{m(\tilde{\chi}_1^\pm) + m(\tilde{\chi}_1^0)\}$. The weak bosons produced in the cascade decays might be offshell, if $\Delta m(\tilde{\chi}_1^\pm, \tilde{\chi}_2^0) < m_W$ or $\Delta m(\tilde{\chi}_2^0, \tilde{\chi}_1^0) < m_Z$. The limits in Figure 7(b) are set for pair-production of gluinos in an R-parity violating scenario (Figure 1(d)) where gluinos decay via top squarks into tbd or tbs final states (experimentally indistinguishable) when λ''_{313} or λ''_{323} couplings are non-zero. Sensitivity to these two scenarios is provided respectively by the SRs Rpc2L0b and Rpv2L, and allows excluding gluino masses below 1.6 TeV for $\tilde{\chi}_1^0$ masses up to 1 TeV or $\tilde{t}_1$ masses up to 1.2 TeV. For gluino masses around the exclusion limits, the signal $\mathcal{A} \times \epsilon$ is up to 0.9% for Rpc2L0b and up to 0.7% for Rpv2L.

Exclusion limits on the masses of third-generation squarks are shown in Figure 8. The limits in Figure 8(a) are set for pair-production of bottom squarks in an R-parity conserving scenario (Figure 1(a)) with decoupled gluinos and squarks from other flavours, with $\tilde{b}_1$ squarks decaying via an intermediate $\tilde{\chi}_1^\pm$ into a top quark, a W boson and the LSP $\tilde{\chi}_1^0$. The mass of the charginos $\tilde{\chi}_1^\pm$ are assumed equal to $m(\tilde{\chi}_1^0) + 100$ GeV. For each point of the $\{m(\tilde{b}_1), m(\tilde{\chi}_1^0)\}$ parameter space, the SR providing the best expected sensitivity among Rpc2L1b and Rpc2L2b is chosen. The former provides sensitivity over most of the plane, while the latter provides some complementarity in the low-$m(\tilde{\chi}_1^0)$ region. The transition between the two regions can be seen as an edge in the exclusion limit. The limits in Figure 8(b) are set for pair-production of top squarks (Figure 1(b)) decaying into a top quark, a chargino and a W boson via a neutralino $\tilde{\chi}_2^0$. The masses are chosen similarly to Ref. [52] such that $m(\tilde{t}_1) = m(\tilde{\chi}_2^0) + m_t = m(\tilde{\chi}_1^0) + 275$ GeV to suppress $\tilde{\chi}_2^0 \to H\tilde{\chi}_1^0$ and have $\tilde{\chi}_2^0 \to W^\mp \tilde{\chi}_1^\pm$ as the dominant decay mode, and $m(\tilde{\chi}_1^\pm) \approx m(\tilde{\chi}_1^0)$ such that decay products of the former into the LSP $\tilde{\chi}_1^0$ are invisible. Upper limits on the production cross-section are provided as a function of the $\tilde{t}_1$ mass; top squarks with masses up to 750 GeV are excluded. For squark masses around

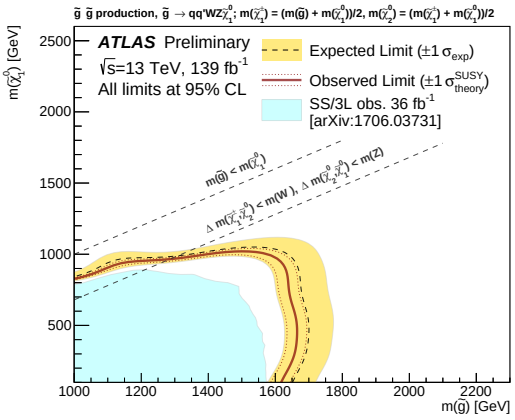

(a) Rpc2L0b: $\tilde{g} \to qq'WZ\tilde{\chi}_1^0$

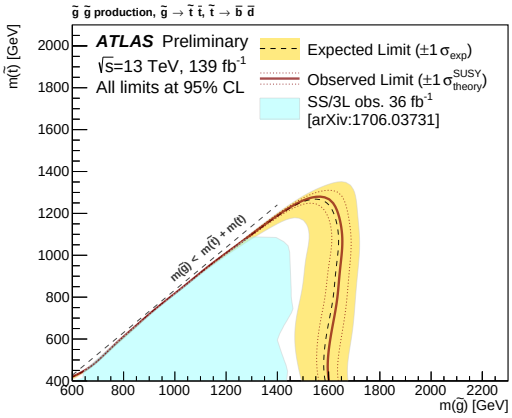

(b) Rpv2L: $\tilde{g} \to t\bar{b}\bar{d}$

Figure 7: 95% confidence level exclusion limits on the production of pairs of gluinos, assuming production cross-sections as in Ref. [27] and 100% branching ratios into the decay modes illustrated respectively in Figures 1(c) and 1(d) for the left and right plots. The limits are determined from the expected contributions of these processes to the Rpc2L0b (left) and Rpv2L (right) SRs. The coloured bands display the $\pm 1\sigma$ ranges of the expected fluctuations around the mean expected limit, in the absence of contributions from the sought-for signals. They do not account for uncertainties in the signal process cross-sections, the impact of which is illustrated by the dashed lines around the observed limits. The figures show for reference the reach of the previous analysis [28].

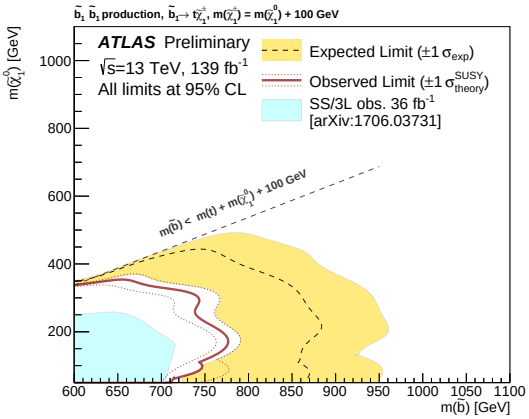

(a) Rpc2L1b+Rpc2L2b: $\tilde{b}_1 \to tW^-\tilde{\chi}_1^0$

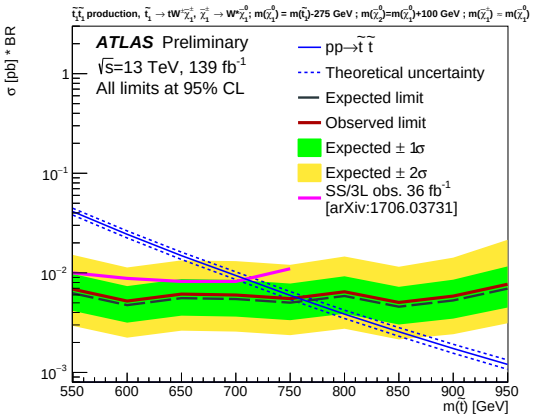

(b) Rpc3LSS1b: $\tilde{t}_1 \to tW^{\mp}\tilde{\chi}_1^{\pm}$

Figure 8: 95% confidence level exclusion limits on the production of pairs of third-generation squarks, assuming production cross-sections as in Ref. [27] (for the left plot) and 100% branching ratios into the decay modes illustrated respectively in Figures 1(a) and 1(b) for the left and right plots. The limits are determined from the expected contributions of these processes to the Rpc2L1b and Rpc2L2b (left) and Rpc3LSS1b (right) SRs. The coloured bands display the $\pm 1\sigma$ ranges (as well as $\pm 2\sigma$ for the right figure) of the expected fluctuations around the mean expected limit, in the absence of contributions from the sought-for signals. They do not account for uncertainties in the signal process cross-sections, the impact of which is illustrated by the dashed lines around the observed limits. The figures show for reference the reach of the previous analysis [28].

the exclusion limit, the signal $\mathcal{A} \times \epsilon$ is up to 0.2% for Rpc2L1b as well as Rpc2L2b, and close to 0.1% for Rpc3LSS1b.

9 Conclusion

A search for supersymmetry in events with same-sign leptons and jets is presented. The analysis is performed with pp collision data collected at a centre-of-mass energy of $\sqrt{s} = 13$ TeV between 2015 and 2018 with the ATLAS detector at the LHC, corresponding to an integrated luminosity of 139 fb^{-1}. Five signal regions are defined to cover a broad range of supersymmetric process signatures. With no significant excess over the SM prediction, results are interpreted in the framework of four simplified models featuring pair production of gluinos or third-generation squarks.

Lower limits on particle masses are derived at 95% confidence level for these models, reaching up to 1.6 TeV for gluinos and 750 GeV for bottom and top squarks, significantly extending the previous exclusion limits obtained with a similar search [28] for a smaller dataset. Model-independent limits on the cross-section of possible BSM signal contributions to the SRs are also reported.

References

[1] R. M. Barnett, J. F. Gunion and H. E. Haber, *Discovering supersymmetry with like-sign dileptons*, Phys. Lett. B **315** (1993) 349, arXiv: hep-ph/9306204.

[2] J. Alwall, R. Frederix, S. Frixione, V. Hirschi, F. Maltoni et al., *The automated computation of tree-level and next-to-leading order differential cross sections, and their matching to parton shower simulations*, JHEP **07** (2014) 079, arXiv: 1405.0301 [hep-ph].

[3] M. Tanabashi et al. (Particle Data Group), *The Review of Particle Physics*, Phys. Rev. D **98** (2018) 030001.

[4] L. Evans and P. Bryant, *LHC Machine*, JINST **3** (2008) S08001.

[5] ATLAS Collaboration, *The ATLAS Experiment at the CERN Large Hadron Collider*, JINST **3** (2008) S08003.

[6] CMS Collaboration, *The CMS experiment at the CERN LHC*, JINST **3** (2008) S08004.

[7] Y. A. Gol'fand and E. P. Likhtman, *Extension of the Algebra of Poincare Group Generators and Violation of P invariance*, JETP Lett. **13** (1971) 323, Erratum: Y. A. Golfand and E. P. Likhtman, Pisma Zh. Eksp. Teor. Fiz. **13** (1971) 452.

[8] D. V. Volkov and V. P. Akulov, *Is the neutrino a goldstone particle?*, Phys. Lett. B **46** (1973) 109.

[9] J. Wess and B. Zumino, *Supergauge transformations in four dimensions*, Nucl. Phys. B **70** (1974) 39.

[10] J. Wess and B. Zumino, *Supergauge invariant extension of quantum electrodynamics*, Nucl. Phys. B **78** (1974) 1.

[11] S. Ferrara and B. Zumino, *Supergauge invariant Yang-Mills theories*, Nucl. Phys. B **79** (1974) 413.

[12] A. Salam and J. A. Strathdee, *Super-symmetry and non-Abelian gauges*, Phys. Lett. B **51** (1974) 353.

[13] N. Sakai, *Naturalness in Supersymmetric GUTs*, Z. Phys. C **11** (1981) 153.

[14] S. Dimopoulos, S. Raby and F. Wilczek, *Supersymmetry and the scale of unification*, Phys. Rev. D **24** (1981) 1681.

[15] L. E. Ibáñez and G. G. Ross, *Low-energy predictions in supersymmetric grand unified theories*, Phys. Lett. B **105** (1981) 439.

[16] S. Dimopoulos and H. Georgi, *Softly broken supersymmetry and SU(5)*, Nucl. Phys. B **193** (1981) 150.

[17] P. Fayet, *Supersymmetry and weak, electromagnetic and strong interactions*, Phys. Lett. B **64** (1976) 159.

[18] P. Fayet, *Spontaneously broken supersymmetric theories of weak, electromagnetic and strong interactions*, Phys. Lett. B **69** (1977) 489.

[19] H. Goldberg, *Constraint on the Photino Mass from Cosmology*, Phys. Rev. Lett. **50** (1983) 1419, Erratum: Phys. Rev. Lett. **103** (2009) 099905.

[20] J. R. Ellis, J. S. Hagelin, D. V. Nanopoulos, K. A. Olive and M. Srednicki, *Supersymmetric relics from the big bang*, Nucl. Phys. B **238** (1984) 453.

[21] G. R. Farrar and P. Fayet, *Phenomenology of the production, decay, and detection of new hadronic states associated with supersymmetry*, Phys. Lett. B **76** (1978) 575.

[22] S. P. Martin, *A Supersymmetry Primer*, Adv. Ser. Direct. High Energy Phys. **18** (1998) 1, arXiv: hep-ph/9709356.

[23] R. Barbieri and G. F. Giudice, *Upper bounds on supersymmetric particle masses*, Nucl. Phys. B **306** (1988) 63.

[24] B. de Carlos and J. A. Casas, *One-loop analysis of the electroweak breaking in supersymmetric models and the fine-tuning problem*, Phys. Lett. B **309** (1993) 320, arXiv: hep-ph/9303291.

[25] K. Inoue, A. Kakuto, H. Komatsu and S. Takeshita, *Aspects of Grand Unified Models with Softly Broken Supersymmetry*, Prog. Theor. Phys. **68** (1982) 927, Erratum: Prog. Theor. Phys. **70** (1983) 330.

[26] J. R. Ellis and S. Rudaz, *Search for supersymmetry in toponium decays*, Phys. Lett. B **128** (1983) 248.

[27] W. Beenakker, C. Borschensky, M. Krämer, A. Kulesza and E. Laenen, *NNLL-fast: predictions for coloured supersymmetric particle production at the LHC with threshold and Coulomb resummation*, JHEP **12** (2016) 133, arXiv: 1607.07741 [hep-ph].

[28] ATLAS Collaboration, *Search for supersymmetry in final states with two same-sign or three leptons and jets using* $36\,fb^{-1}$ *of* $\sqrt{s} = 13$ *TeV pp collision data with the ATLAS detector*, JHEP **09** (2017) 084, arXiv: 1706.03731 [hep-ex].

[29] CMS Collaboration, *Search for physics beyond the standard model in events with two leptons of same sign, missing transverse momentum, and jets in proton–proton collisions at* $\sqrt{s} = 13$ *TeV*, Eur. Phys. J. C **77** (2017) 578, arXiv: 1704.07323 [hep-ex].

[30] CMS Collaboration, *Search for supersymmetry in events with at least three electrons or muons, jets, and missing transverse momentum in proton–proton collisions at* $\sqrt{s} = 13$ *TeV*, JHEP **02** (2018) 067, arXiv: 1710.09154 [hep-ex].

[31] ATLAS Collaboration, *ATLAS Insertable B-Layer Technical Design Report*, ATLAS-TDR-19, 2010, URL: https://cds.cern.ch/record/1291633, Addendum: ATLAS-TDR-19-ADD-1, 2012, URL: https://cds.cern.ch/record/1451888.

[32] ATLAS Collaboration, *Production and integration of the ATLAS Insertable B-Layer*, JINST **13** (2018) T05008, arXiv: 1803.00844 [physics.ins-det].

[33] ATLAS Collaboration, *Luminosity determination in pp collisions at* $\sqrt{s} = 8$ *TeV using the ATLAS detector at the LHC*, Eur. Phys. J. C **76** (2016) 653, arXiv: 1608.03953 [hep-ex].

[34] G. Avoni et al., *The new LUCID-2 detector for luminosity measurement and monitoring in ATLAS*, JINST **13** (2018) P07017.

[35] ATLAS Collaboration, *Vertex Reconstruction Performance of the ATLAS Detector at* $\sqrt{s} = 13$ *TeV*, ATL-PHYS-PUB-2015-026, 2015, URL: https://cds.cern.ch/record/2037717.

[36] ATLAS Collaboration, *Reconstruction of primary vertices at the ATLAS experiment in Run 1 proton–proton collisions at the LHC*, Eur. Phys. J. C **77** (2017) 332, arXiv: 1611.10235 [hep-ex].

[37] M. Cacciari, G. P. Salam and G. Soyez, *The anti-k_t jet clustering algorithm*, JHEP **04** (2008) 063, arXiv: 0802.1189 [hep-ph].

[38] M. Cacciari, G. P. Salam and G. Soyez, *FastJet User Manual*, Eur. Phys. J. C **72** (2012) 1896, arXiv: 1111.6097 [hep-ph].

[39] ATLAS Collaboration, *Topological cell clustering in the ATLAS calorimeters and its performance in LHC Run 1*, Eur. Phys. J. C **77** (2017) 490, arXiv: 1603.02934 [hep-ex].

[40] ATLAS Collaboration, *Jet energy scale measurements and their systematic uncertainties in proton–proton collisions at* $\sqrt{s} = 13$ *TeV with the ATLAS detector*, Phys. Rev. D **96** (2017) 072002, arXiv: 1703.09665 [hep-ex].

[41] ATLAS Collaboration, *Selection of jets produced in* 13 *TeV proton–proton collisions with the ATLAS detector*, ATLAS-CONF-2015-029, 2015, URL: https://cds.cern.ch/record/2037702.

[42] ATLAS Collaboration, *Performance of pile-up mitigation techniques for jets in pp collisions at* $\sqrt{s} = 8$ *TeV using the ATLAS detector*, Eur. Phys. J. C **76** (2016) 581, arXiv: 1510.03823 [hep-ex].

[43] ATLAS Collaboration, *Measurements of b-jet tagging efficiency with the ATLAS detector using* $t\bar{t}$ *events at* $\sqrt{s} = 13$ *TeV*, JHEP **08** (2018) 089, arXiv: 1805.01845 [hep-ex].

[44] ATLAS Collaboration, *Muon reconstruction performance of the ATLAS detector in proton–proton collision data at* $\sqrt{s} = 13$ *TeV*, Eur. Phys. J. C **76** (2016) 292, arXiv: 1603.05598 [hep-ex].

[45] ATLAS Collaboration, *Electron reconstruction and identification in the ATLAS experiment using the 2015 and 2016 LHC proton–proton collision data at* $\sqrt{s} = 13$ *TeV*, CERN-EP-2018-273 (2019), arXiv: 1902.04655 [hep-ex].

[46] ATLAS Collaboration, *Measurement of the photon identification efficiencies with the ATLAS detector using LHC Run 2 data collected in 2015 and 2016*, Eur. Phys. J. C **79** (2019) 205, arXiv: 1810.05087 [hep-ex].

[47] ATLAS Collaboration, *Performance of missing transverse momentum reconstruction with the ATLAS detector using proton–proton collisions at* $\sqrt{s} = 13$ *TeV*, Eur. Phys. J. C **78** (2018) 903, arXiv: 1802.08168 [hep-ex].

[48] ATLAS Collaboration, E_T^{miss} *performance in the ATLAS detector using 2015–2016 LHC pp collisions*, ATLAS-CONF-2018-023, 2018, URL: https://cds.cern.ch/record/2625233.

[49] ATLAS Collaboration, *2015 start-up trigger menu and initial performance assessment of the ATLAS trigger using Run-2 data*, ATL-DAQ-PUB-2016-001, 2016, URL: https://cds.cern.ch/record/2136007.

[50] ATLAS Collaboration, *Trigger Menu in 2016*, ATL-DAQ-PUB-2017-001, 2017, URL: https://cds.cern.ch/record/2242069.

[51] ATLAS Collaboration, *Trigger Menu in 2017*, ATL-DAQ-PUB-2018-002, 2018, URL: https://cds.cern.ch/record/2625986.

[52] P. Huang, A. Ismail, I. Low and C. E. M. Wagner, *Same-Sign dilepton excesses and light top squarks*, Phys. Rev. D **92** (2015) 075035, arXiv: 1507.01601 [hep-ph].

[53] ATLAS Collaboration, *Modelling of the vector boson scattering process $pp \to W^{\pm}W^{\pm}jj$ in Monte Carlo generators in ATLAS*, ATL-PHYS-PUB-2019-004, 2019, URL: https://cds.cern.ch/record/2655303.

[54] ATLAS Collaboration, *Modelling of the $t\bar{t}H$ and $t\bar{t}V(V = W, Z)$ processes for $\sqrt{s} = 13$ TeV ATLAS analyses*, ATL-PHYS-PUB-2016-005, 2016, URL: https://cds.cern.ch/record/2120826.

[55] T. Sjöstrand et al., *An introduction to PYTHIA 8.2*, Comput. Phys. Commun. **191** (2015) 159, arXiv: 1410.3012 [hep-ph].

[56] D. de Florian et al., *Handbook of LHC Higgs cross sections: 4. Deciphering the nature of the Higgs sector*, CERN-2017-002-M (2016), arXiv: 1610.07922 [hep-ph].

[57] R. D. Ball et al., *Parton distributions with LHC data*, Nucl. Phys. B **867** (2013) 244, arXiv: 1207.1303 [hep-ph].

[58] ATLAS Collaboration, *ATLAS Pythia 8 tunes to 7 TeV data*, ATL-PHYS-PUB-2014-021, 2014, URL: https://cds.cern.ch/record/1966419.

[59] T. Sjöstrand, S. Mrenna and P. Z. Skands, *A brief introduction to PYTHIA 8.1*, Comput. Phys. Commun. **178** (2008) 852, arXiv: 0710.3820 [hep-ph].

[60] P. Nason, *A new method for combining NLO QCD with shower Monte Carlo algorithms*, JHEP **11** (2004) 040, arXiv: hep-ph/0409146.

[61] ATLAS Collaboration, *Multi-Boson Simulation for 13 TeV ATLAS Analyses*, ATL-PHYS-PUB-2017-005, 2017, URL: https://cds.cern.ch/record/2261933.

[62] T. Gleisberg et al., *Event generation with SHERPA 1.1*, JHEP **02** (2009) 007, arXiv: 0811.4622 [hep-ph].

[63] R. D. Ball et al., *Parton distributions for the LHC run II*, JHEP **04** (2015) 040, arXiv: 1410.8849 [hep-ph].

[64] ATLAS Collaboration, *The ATLAS Simulation Infrastructure*, Eur. Phys. J. C **70** (2010) 823, arXiv: 1005.4568 [physics.ins-det].

[65] S. Agostinelli et al., *GEANT4 — a simulation toolkit*, Nucl. Instrum. Meth. A **506** (2003) 250.

[66] ATLAS Collaboration, *The Pythia 8 A3 tune description of ATLAS minimum bias and inelastic measurements incorporating the Donnachie–Landshoff diffractive model*, ATL-PHYS-PUB-2016-017, 2016, URL: https://cds.cern.ch/record/2206965.

[67] D. J. Lange, *The EvtGen particle decay simulation package*, Nucl. Instrum. Meth. A **462** (2001) 152.

[68] J. Butterworth et al., *PDF4LHC recommendations for LHC Run II*, J. Phys. G **43** (2016) 023001, arXiv: 1510.03865 [hep-ph].

[69] S. Höche, F. Krauss, S. Schumann and F. Siegert, *QCD matrix elements and truncated showers*, JHEP **05** (2009) 053, arXiv: 0903.1219 [hep-ph].

[70] S. Höche, S. Schumann and F. Siegert, *Hard photon production and matrix-element parton-shower merging*, Phys. Rev. D **81** (2010) 034026, arXiv: 0912.3501 [hep-ph].

[71] S. Schumann and F. Krauss, *A parton shower algorithm based on Catani-Seymour dipole factorisation*, JHEP **03** (2008) 038, arXiv: 0709.1027 [hep-ph].

[72] B. Humpert and R. Odorico, *Multi-parton scattering and QCD radiation as sources of four-jet events*, Phys. Lett. B **154** (1985) 211.

[73] D. Treleani, *Double parton scattering, diffraction, and effective cross section*, Phys. Rev. D **76** (2007) 076006, arXiv: 0708.2603 [hep-ph].

[74] ATLAS Collaboration, *Study of multiple hard-scatter processes from different p p interactions in the same ATLAS event*, ATL-PHYS-PUB-2018-007, 2018, URL: http://cdsweb.cern.ch/record/2320419.

[75] J. R. Gaunt, C.-H. Kom, A. Kulesza and W. J. Stirling, *Same-sign W pair production as a probe of double-parton scattering at the LHC*, Eur. Phys. J. C **69** (2010) 53, arXiv: 1003.3953 [hep-ph].

[76] P. Onyisi and A. Webb, *Impact of rare decays $t \to \ell'\nu b\ell\ell$ and $t \to qq'b\ell\ell$ on searches for top-associated physics*, JHEP **02** (2018) 156, arXiv: 1704.07343 [hep-ph].

[77] N. Davidson, T. Przedzinski and Z. Was, *PHOTOS Interface in C++: Technical and Physics Documentation*, (2010), arXiv: 1011.0937 [hep-ph].

[78] ATLAS Collaboration, *Search for supersymmetry at $\sqrt{s} = 8$ TeV in final states with jets and two same-sign leptons or three leptons with the ATLAS detector*, JHEP **06** (2014) 035, arXiv: 1404.2500 [hep-ex].

[79] M. Baak et al., *HistFitter software framework for statistical data analysis*, Eur. Phys. J. C **75** (2015) 153, arXiv: 1410.1280 [hep-ex].

[80] G. Cowan, K. Cranmer, E. Gross and O. Vitells, *Asymptotic formulae for likelihood-based tests of new physics*, Eur. Phys. J. C **71** (2011) 1554, arXiv: 1007.1727 [physics.data-an], Erratum: Eur. Phys. J. C **73** (2013) 2501.

[81] A. L. Read, *Presentation of search results: the CL_S technique*, J. Phys. G **28** (2002) 2693.

[82] J. Alwall, M.-P. Le, M. Lisanti and J. G. Wacker, *Searching for directly decaying gluinos at the Tevatron*, Phys. Lett. B **666** (2008) 34, arXiv: 0803.0019 [hep-ph].

[83] J. Alwall, P. Schuster and N. Toro, *Simplified models for a first characterization of new physics at the LHC*, Phys. Rev. D **79** (2009) 075020, arXiv: 0810.3921 [hep-ph].

[84] D. Alves et al., *Simplified models for LHC new physics searches*, J. Phys. G **39** (2012) 105005, arXiv: 1105.2838 [hep-ph].

[85] L. Lönnblad and S. Prestel, *Matching tree-level matrix elements with interleaved showers*, JHEP **03** (2012) 019, arXiv: 1109.4829 [hep-ph].

[86] ATLAS Collaboration, *The simulation principle and performance of the ATLAS fast calorimeter simulation FastCaloSim*, ATL-PHYS-PUB-2010-013, 2010, URL: https://cds.cern.ch/record/1300517.

[87] M. Beneke, M. Czakon, P. Falgari, A. Mitov and C. Schwinn, *Threshold expansion of the $gg(q\bar{q}) \to Q\bar{Q} + X$ cross section at $O(\alpha_s^4)$*, Phys. Lett. B **690** (2010) 483, arXiv: 0911.5166 [hep-ph].